



AFRL-RQ-WP-TP-2017-0167

HIGH-SPEED SCHLIEREN AND 10-HZ KR PLIF FOR THE NEW AFRL MACH 6 LUDWIEG TUBE HYPERSONIC WIND TUNNEL

**Roger L. Kimmel and Campbell D. Carter
Hypersonic Sciences Branch
High Speed Systems Division**

**Joshua D. Pickles and Venkateswaran Narayanaswamy
North Carolina State University**

**King-Yiu Lam
Spectral Energies, LLC**

**NOVEMBER 2017
Interim Report**

**DISTRIBUTION STATEMENT A: Approved
for public release. Distribution is unlimited.**

**AIR FORCE RESEARCH LABORATORY
AEROSPACE SYSTEMS DIRECTORATE
WRIGHT-PATTERSON AIR FORCE BASE, OH 45433-7542
AIR FORCE MATERIEL COMMAND
UNITED STATES AIR FORCE**

NOTICE AND SIGNATURE PAGE

Using Government drawings, specifications, or other data included in this document for any purpose other than Government procurement does not in any way obligate the U.S. Government. The fact that the Government formulated or supplied the drawings, specifications, or other data does not license the holder or any other person or corporation; or convey any rights or permission to manufacture, use, or sell any patented invention that may relate to them.

This report was cleared for public release by the USAF 88th Air Base Wing (88 ABW) Public Affairs Office (PAO) and is available to the general public, including foreign nationals.

Copies may be obtained from the Defense Technical Information Center (DTIC)
(<http://www.dtic.mil>).

AFRL-RQ-WP-TP-2017-0167 has been reviewed and is approved for publication in accordance with assigned distribution statement.

REPORT DOCUMENTATION PAGE

*Form Approved
OMB No. 0704-0188*

The public reporting burden for this collection of information is estimated to average 1 hour per response, including the time for reviewing instructions, searching existing data sources, gathering and maintaining the data needed, and completing and reviewing the collection of information. Send comments regarding this burden estimate or any other aspect of this collection of information, including suggestions for reducing this burden, to Department of Defense, Washington Headquarters Services, Directorate for Information Operations and Reports (0704-0188), 1215 Jefferson Davis Highway, Suite 1204, Arlington, VA 22202-4302. Respondents should be aware that notwithstanding any other provision of law, no person shall be subject to any penalty for failing to comply with a collection of information if it does not display a currently valid OMB control number. **PLEASE DO NOT RETURN YOUR FORM TO THE ABOVE ADDRESS.**

1. REPORT DATE (DD-MM-YY) November 2017			2. REPORT TYPE Interim		3. DATES COVERED (From - To) 26 February 2015 – 01 July 2017			
4. TITLE AND SUBTITLE HIGH-SPEED SCHLIEREN AND 10-HZ KR PLIF FOR THE NEW AFRL MACH-6 LUDWIEG TUBE HYPERSONIC WIND TUNNEL			5a. CONTRACT NUMBER In-house					
			5b. GRANT NUMBER					
			5c. PROGRAM ELEMENT NUMBER 61102F					
6. AUTHOR(S) Roger L. Kimmel and Campbell D. Carter (AFRL/RQHF) Joshua D. Pickles and Venkateswaran Narayanaswamy (North Carolina State University) King-Yiu Lam (Spectral Energies, LLC)			5d. PROJECT NUMBER 3002					
			5e. TASK NUMBER					
			5f. WORK UNIT NUMBER Q1FN					
7. PERFORMING ORGANIZATION NAME(S) AND ADDRESS(ES) Hypersonic Sciences Branch High Speed Systems Division Air Force Research Laboratory, Aerospace Systems Directorate Wright-Patterson Air Force Base, OH 45433-7542 Air Force Materiel Command, United States Air Force			8. PERFORMING ORGANIZATION REPORT NUMBER AFRL-RQ-WP-TP-2017-0167					
9. SPONSORING/MONITORING AGENCY NAME(S) AND ADDRESS(ES) Air Force Research Laboratory Aerospace Systems Directorate Wright-Patterson Air Force Base, OH 45433-7542 Air Force Materiel Command United States Air Force			10. SPONSORING/MONITORING AGENCY ACRONYM(S) AFRL/RQHF					
			11. SPONSORING/MONITORING AGENCY REPORT NUMBER(S) AFRL-RQ-WP-TP-2017-0167					
12. DISTRIBUTION/AVAILABILITY STATEMENT DISTRIBUTION STATEMENT A: Approved for public release. Distribution is unlimited.								
13. SUPPLEMENTARY NOTES PA Clearance Number: 88ABW-2016-6075; Clearance Date: 28 Nov 2016								
14. ABSTRACT Flow visualization measurement techniques, namely high-speed schlieren and two-photon Kr planar laser-induced fluorescence (PLIF at 10-Hz repetition rate), were developed and implemented in a new AFRL Mach-6 Ludwieg Tube Hypersonic Wind Tunnel. Because of its high frame rates, the schlieren technique was first employed to image the starting shock and the entire startup process. These schlieren images also helped interpret the pressure measurements during the startup process and characterize the tunnel noise for boundary-layer transition experiments. Next, both schlieren and Kr PLIF were employed to image the bow shock from a large blunt cone at $P_0 = 1.38$ MPa, and the measured bow shock shapes from both techniques were compared to CFD calculations employing the US3D simulation code.								
15. SUBJECT TERMS boundary layer transition, hypersonic, ground test								
16. SECURITY CLASSIFICATION OF: a. REPORT Unclassified			17. LIMITATION OF ABSTRACT: SAR		18. NUMBER OF PAGES 19		19a. NAME OF RESPONSIBLE PERSON (Monitor) Roger L. Kimmel	
b. ABSTRACT Unclassified								
19b. TELEPHONE NUMBER (Include Area Code) N/A								



High-Speed Schlieren and 10-Hz Kr PLIF for the new AFRL Mach-6 Ludwieg Tube Hypersonic Wind Tunnel

King-Yiu Lam¹

Spectral Energies, LLC, Dayton, OH 45431

Joshua D. Pickles², Venkateswaran Narayanaswamy³
North Carolina State University, Raleigh, NC 27695

and

Campbell D. Carter⁴, and Roger L. Kimmel⁵

Air Force Research Laboratory, Wright-Patterson Air Force Base, OH 45433

Flow visualization measurement techniques, namely high-speed schlieren and two-photon Kr planar laser-induced fluorescence (PLIF at 10-Hz repetition rate), were developed and implemented in a new AFRL Mach-6 Ludwieg Tube Hypersonic Wind Tunnel. Because of its high frame rates, the schlieren technique was first employed to image the starting shock and the entire startup process. These schlieren images also helped interpret the pressure measurements during the startup process and characterize the tunnel noise for boundary-layer transition experiments. Next, both schlieren and Kr PLIF were employed to image the bow shock from a large blunt cone at $P_o = 1.38$ MPa, and the measured bow shock shapes from both techniques were compared to CFD calculations employing the US3D simulation code.

Nomenclature

P_o	= stagnation pressure
P	= static pressure
T_o	= stagnation temperature
T	= static temperature
γ	= specific heat ratio
M	= Mach number
ρ	= density
Re	= unit Reynolds number (per meter)
S	= schlieren sensitivity
f	= focal length of the parabolic mirror
a	= width of the unobstructed light-source image in the schlieren cutoff plane
b	= width of the entire light-source image
λ	= wavelength, nm
n	= number density, m^{-3}
y^+	= dimensionless wall distance

I. Introduction

Laminar-turbulent transition in hypersonic boundary layers is critical for prediction and control of heat transfer, skin friction, and other boundary-layer properties. Accurate knowledge of laminar-turbulent

¹ Research Aerospace Engineer, Spectral Energies, LLC, Dayton, OH 45431. AIAA Member.

² Graduate Research Assistant, Department of Mechanical and Aerospace Engineering, Rayleigh, NC 27695. AIAA Student Member.

³ Assistant Professor, Department of Mechanical and Aerospace Engineering, Rayleigh, NC 27695. AIAA Member.

⁴ Principal Aerospace Engineer, AFRL/RQHP, Wright-Patterson AFB, OH 45433. AIAA Associate Fellow.

⁵ Principal Aerospace Engineer, AFRL/RQHF, Wright-Patterson AFB, OH 45433. AIAA Associate Fellow.

transition prediction can help improve aerodynamic lift and drag, aerodynamic stability and control, and the design of the thermal protection system^{1,2}. It remains a great challenge of understanding the transition process in hypervelocity flows ($M > 5$) because of different instability modes for different geometries. The dominant instability is typically the second mode over slender two-dimensional (2-D) or axisymmetric geometries (at a 0-deg. angle of attack) for hypersonic flows³. Traditionally, researchers have used surface sensors, such as pressure sensors, hot wires, and heat-flux gauges, to study the growth of the 2nd mode instability in wind tunnel environment. Recently, several researchers⁴⁻⁸ have implemented high-speed schlieren imaging (using both conventional and focused methods) to investigate the development of second-mode instability waves in the hypersonic boundary layer of a slender cone. These second-mode waves can be observed as some sort of “ropelike” structures from the schlieren images⁴⁻⁷. Also, quantitative measurements, such as the propagation speed and frequency content of the second-mode waves, can be inferred from these high-speed schlieren images.

Planar laser-induced fluorescence (PLIF) is an imaging technique on yielding insight into many aspects of transient supersonic, hypersonic, and reacting environments⁹⁻¹⁶. The common seeded tracer-species for PLIF techniques are nitric oxide (NO), iodine (I₂), vapors of hydrocarbon substances (e.g., acetone and toluene), and krypton (Kr). Recently, an interest in using Kr as a flow tracer has arisen because it is a noble gas (and thus unreactive and easy to mix with other gases) and nontoxic. However, Kr PLIF requires a two-photon excitation at a wavelength near 214.7 nm⁹⁻¹², and thus the absorption cross-section is relatively small (at least for nanosecond-duration laser pulses) and the dependence on laser intensity is quadratic in nature. Nevertheless, researchers^{12,15} have successfully employed two-photon Kr PLIF to study unsteady supersonic flow phenomena in Mach-3 wind tunnels.

This paper focuses on the development of two flow visualization techniques, namely high-speed schlieren and two-photon Kr PLIF (at 10-Hz repetition rate), for a new AFRL Mach-6 Ludwieg Tube Hypersonic Wind Tunnel. Because the freestream density for a Mach-6 flow is rather low, the purpose of this work is to assess the feasibility of using these two techniques on acquiring good and useful signals in a Mach-6 air flow in a configuration of interest (e.g., bow shock, freestream disturbance, and/or boundary layer). The first part of this paper presents some preliminary schlieren imaging results during the start-up process. Because of the high frame rates, a frequency spectrum of the flow disturbances during the run can be inferred from the high-speed images in order to help characterize the tunnel noise. In the second part of this work, both schlieren and two-photon Kr PLIF were used to image the bow shock shape from a large blunt-cone model. To the best of our knowledge, this paper presents the first set of two-photon Kr PLIF measurements in a large scale Mach-6 Ludwieg tube facility. The measured bow shock shapes from both techniques are compared to CFD calculations employing the US3D simulation code.

II. Experimental Setup

Ludwieg Tube Setup

The new AFRL Mach-6 Ludwieg Tube Hypersonic Wind Tunnel was constructed to generate a Mach-6 air flow at various stagnation pressures of 379 kPa – 4.14 MPa, resulting in unit freestream Reynolds numbers of $6.56 \times 10^5 / m - 3.28 \times 10^7 / m$, as shown in Figure 1. More details about the Ludwieg tube facility can be found from ref. 17. The inner surface of the driver tube is heated to 505 K, and the driver tube is connected to a gas heater that heats up the gas from two compressors up to a temperature around 500 K. This tunnel can be run in different modes: a single-diaphragm mode, a double-diaphragm mode, and a fast plug valve mode. Currently, the tunnel is equipped with a pneumatic-driven fast plug valve with an opening time of ~18 ms, thereby generating relatively short, frequent runs (0.1-s test time in every 5 minutes) with low infrastructure cost. Note that some of the images presented in this paper were acquired when the tunnel was operated in a single-diaphragm mode, while others were acquired when the tunnel was operated in a fast plug valve mode. The test chamber has a diameter of approximately 1.27 m and contains three circular hatches, one on the top and one each on the east and west faces of the test chamber. The east hatch is an autoclave door that provides rapid access to the test section. Both east and west hatches contain 30.5-cm diameter fused quartz windows. The top hatch contains a 10.2-cm diameter calcium fluoride window for

infrared measurements. However, for the PLIF measurements, the east-side window was replaced by a smaller (50-mm diam.) high-graded fused silica window (Corning 7980). The transmission for this window was about 90% at 214.7 nm.



Figure 1. AFRL Mach-6 Ludwieg Tube Hypersonic Wind Tunnel.

After the construction of the Ludwieg tube, a 25.4-cm wide Pitot rake was first instrumented and installed at the test section in order to survey the flow conditions. Four Kulite pressure sensors (spaced at 8.26-cm apart from each other) were installed on the Pitot rake and were used to measure the stagnation pressures (P_{o2}) behind the bow shock and survey the spanwise Mach uniformity. Three of these sensors (model #: XTEL-190-25A) were flush-mounted onto the surface, and the last sensor (sensor #3; model #: XCEL-100-0.35BARA) was protruded from the surface (about 2.5 cm), as illustrated in Figure 2.

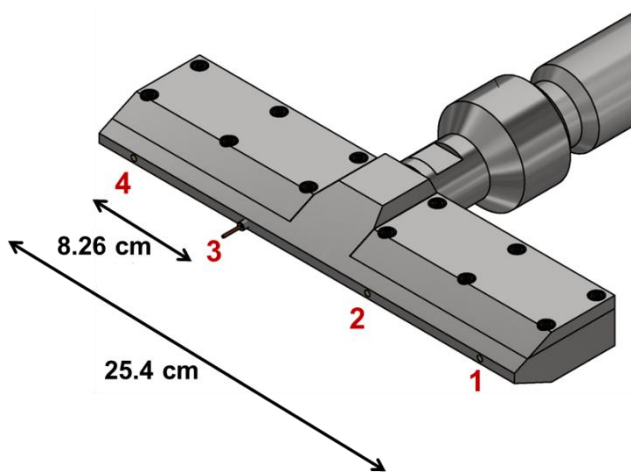


Figure 2. Schematic of Pitot rake at the test section.

In addition to the Pitot pressure measurements, a series of Kulite pressure sensors were installed at various locations of the Ludwieg tube to survey the flow conditions of the tunnel and to determine the flow Mach number. Figure 3 shows the pressure time histories for three sensors, namely nozzle entrance pressure (P_{o1}), nozzle exit pressure (P_1), and Pitot pressure sensor #3 (P_{o2} , the sensor protruding from the surface), for the 621-kPa test run at a stagnation temperature of $T_o \approx 500$ K. As illustrated in Figure 3, once the tunnel started, a nearly uniform pressure region was achieved over a period of 100-ms. Shortly after this quasi-steady period, a small pressure drop at $t \approx 120\text{-}135$ ms was observed due to the arrival of the expansion

fan reflected from the driver endwall, followed by another 100-ms quasi-steady period. After that, the tunnel unstarted at $t = 240$ ms.

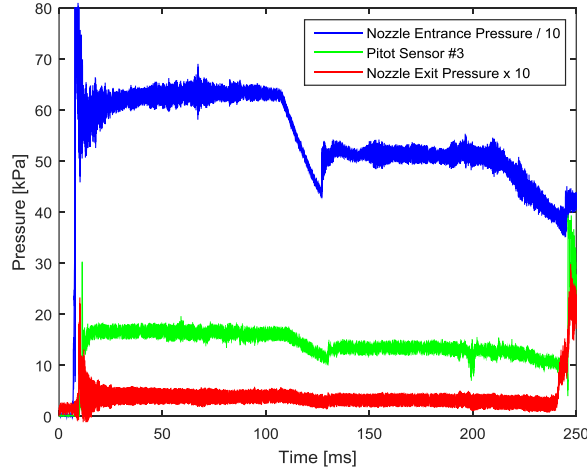


Figure 3. Pressure time histories at nozzle entrance, nozzle exit, and Pitot rake for the 621-kPa run.

The flow Mach number can be determined using the normal shock relation:

$$\frac{P_{o2}}{P_{o1}} = \left[\frac{(\gamma+1)M_1^2}{(\gamma-1)M_1^2+2} \right]^{\frac{\gamma}{\gamma-1}} \left[\frac{\gamma+1}{2\gamma M_1^2 - (\gamma-1)} \right]^{\frac{1}{\gamma-1}} \quad (1)$$

where $\gamma = 1.4$ for air, M_1 is the flow Mach number (at the upstream of the bow shock), P_1 is the nozzle exit pressure, P_{o1} is the nozzle entrance pressure, and P_{o2} is the Pitot pressure sensor 3 from the rake. Figure 4 shows the computed Mach number using Eq. (1), and the computed flow Mach number was found to be about 6.10 for this 621-kPa test run. As stated in ref. 17, a good spanwise Mach uniformity can be obtained during the tunnel runs. Note that there was a large spike occurred at $t = 200$ ms (as illustrated in Figures 3 and 4), which was caused, presumably, by the particle impact on the Pitot sensor.

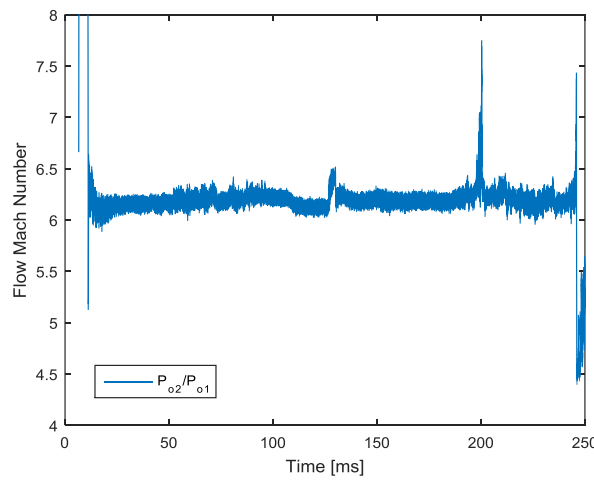


Figure 4. Flow Mach number determination for the 621-kPa run.

After confirming the Mach-6 flow, the next step is to investigate how large of a model can be used at the test section without unstarting the tunnel. In the present study, a large 19.5-deg. half-angle blunt cone was designed and installed at the test section. As shown in Figure 5, the blunt cone has a nose radius of 3.96 cm, a total length of 31.8 cm, and a base diameter of 28.7 cm. This cone is comprised of two sections. The first cone section is made of a polymer with a length of 24.2 cm and a base diameter of 23.2 cm. The

second frustum section is made of stainless steel with a length of 7.62 cm. High-speed schlieren and two-photon Kr PLIF are implemented to help determine if the tunnel can successfully start when this large model is installed. The imaging results will be presented in the next section.

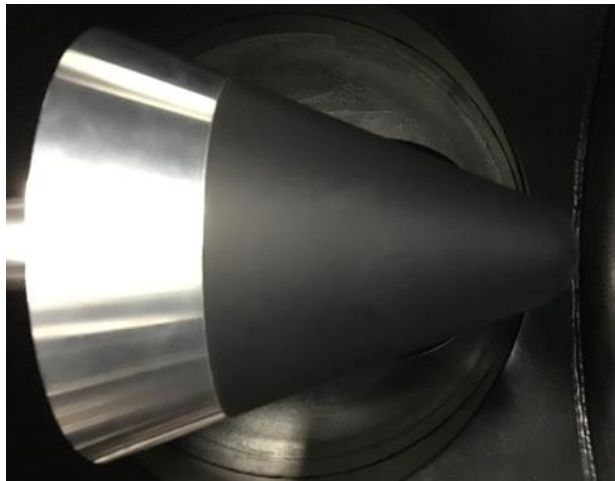


Figure 5. Blunt cone (blockage model) installed at the test section.

High-Speed Schlieren System

The high-speed schlieren system was based on a Z-type configuration, consisting of a pair of matched high f/#, parabolic mirrors (31.8-cm diam. \times 1.91-m focal length with a surface accuracy of $\lambda/8$) and a set of flat mirrors ($\lambda/10$). Long focal-length parabolic mirrors are preferred in order to enhance the schlieren sensitivity (S), governed by:

$$S = \frac{f_2}{a} = \frac{f_2}{b\left(1 - \frac{\%cutoff}{100}\right)} \quad (2)$$

where f_2 is the focal length of the second parabolic mirror, a is the width of the unobstructed light-source image in the schlieren cutoff plane, and b is the width of the entire light-source image^{18,19}. A 250-W Quartz-Tungsten-Halogen (QTH) lamp with a condenser lens and a 1.5-mm wide vertical slit was used as an extended light source in the present study. In addition, a Photron SA-Z camera with a 180-mm f/2.8 camera lens was used to register the schlieren images in this study. A 50% vertical cutoff was also selected to enhance the schlieren sensitivity in the horizontal direction.

Two-Photon Kr PLIF Setup

Research-grade Kr (99.995%) was employed for all measurements. For a run at $P_0 = 1.38$ MPa, a partial pressure of 34.5-kPa Kr was seeded with the hot air in the driver tube, resulting in a gas mixture of 2.5% Kr in air. Each 2000-L Kr bottle can support about eight 1.38-MPa runs. The same approach of Narayanaswamy et al.⁹ and Hsu et al.¹⁰ was followed to pump the $5p[3/2]_2 \leftarrow 4p^{61}S_0$ transition of Kr with a two-photon absorption process excited by 214.7-nm light. Fluorescence is obtained when the electronically-excited atoms transition to either the $5s[3/2]_2$ (71%) or $5s[3/2]_1$ (29%) states, with radiation at 760 nm or 819 nm, respectively. The fluorescence lifetime of the upper level is about 25.4 ns¹⁰. The Kr PLIF experimental setup for the Mach-6 Ludwieg tube is shown in Fig. 6. The laser system consisted of an injection-seeded Nd:YAG laser (Spectra-Physics GCR-170 running at 10 Hz), producing frequency-doubled ($\lambda = 532$ nm with 220 mJ/pulse) and tripled ($\lambda = 355$ nm with 190 mJ/pulse) outputs and a tunable dye laser (Lumonics HD-300) operated with Fluorescein 548 dye (which was *base shifted* with the addition of NaOH). The dye laser was pumped with the frequency-doubled Nd:YAG beam and produced an output near 544 nm (with 21 mJ/pulse). The dye laser beam was then sum-frequency mixed with the 355-nm Nd:YAG beam (within a β -barium borate, BBO, crystal) to produce 8-ns duration pulses near 214.7 nm for exciting Kr. Prior to the Ludwieg tube runs, there were trace amounts of Kr remaining in the test section

(from the previous run), and the wavelength of the dye laser beam was first confirmed with a wavemeter, followed by scanning the dye laser in small, incremental steps and seeking for the brightest fluorescence signals collected by the camera to ensure that the light was at the peak of the Kr absorption line. The existing laser configuration had been proven to produce a 13-mJ UV light near 214.7 nm. Unfortunately, the injection seeder was not performing well in this work, so that the 214.7-nm laser beam had an energy of only 3-5 mJ/pulse (with a linewidth of 0.187 cm^{-1} measured by the wavemeter). The excitation beam was formed into a 7.1-mm or 2.8-cm wide collimated sheet using the combination of a cylindrical concave lens ($f = -500\text{ mm}$ or -200 mm , respectively) and a spherical convex lens ($f = 1\text{ m}$). The sheet was focused at the center-plane of the blunt-cone model installed at the test section of the tunnel, and the thickness of the sheet at focus was measured to be less than 0.5 mm with small variation across the imaging area. The fluorescence signals from both emission lines at 760 and 819 nm were imaged using a 14-bit back-illuminated, EMCCD (Andor) camera with a Nikon 85-mm f/1.8 camera lens; for this camera, near-IR quantum efficiency is expected to be $\sim 80\%$. The images were recorded in a 512×512 pixel window format with a 2×2 binning, resulting in a spatial resolution of 0.357 mm/pixel.

In the present study, a horizontal laser sheet was directed through the east-side window of the test section, and the fluorescence signals were detected by the camera mounted at the top (as shown in Figure 6).

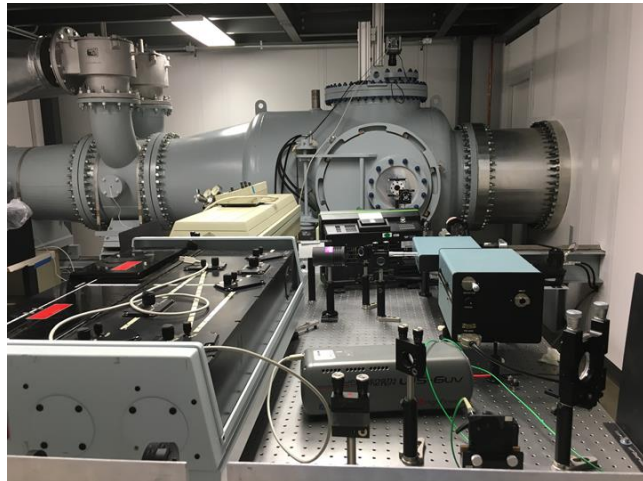


Figure 6. Two-photon Kr PLIF experimental setup.

III. Results and Discussion

Schlieren Imaging Results for the Pitot Rake during the Start-up Process at $P_o = 621\text{ kPa}$

High-speed schlieren is the first flow visualization technique implemented in the Mach-6 Ludwieg tube. The 25.4-cm wide Pitot rake was first instrumented and installed (in the horizontal orientation) at the test section of the tunnel. Note that the tunnel was operated in a single-diaphragm mode for these Pitot rake runs. For the 621-kPa test run, the frame rate of the Photron SA-Z camera was set at 30,000 fps with a shutter time of 2.5 μs . The pixel window area was set at 1024×688 , which covered an observation area with a diameter of 21.3 cm. Note that the spatial resolution was 0.195 mm/pixel. Figure 7 shows the schlieren images that capture the movement of the starting shock from right to left (starting from Frame 2 to Frame 6). It should also be noted that there was some small anomaly on one of the fused quartz windows, resulting in blur on the lower right corner of each image. The Pitot sensor #3 was attached to the Pitot rake on these images, and the frame numbers are also provided on the upper right corner of each image. Note that each frame interval is 33.3 μs . Hence, it took about 0.20 ms for the starting shock to travel a distance of approximately 21.3 cm, yielding a shock speed of about 1064 m/s. In particular, Frames 2-6 illustrate the interaction between the starting shock and the Pitot rake. Frame 6 illustrates how the starting shock was reflected from the Pitot probe before the tunnel flow became supersonic.

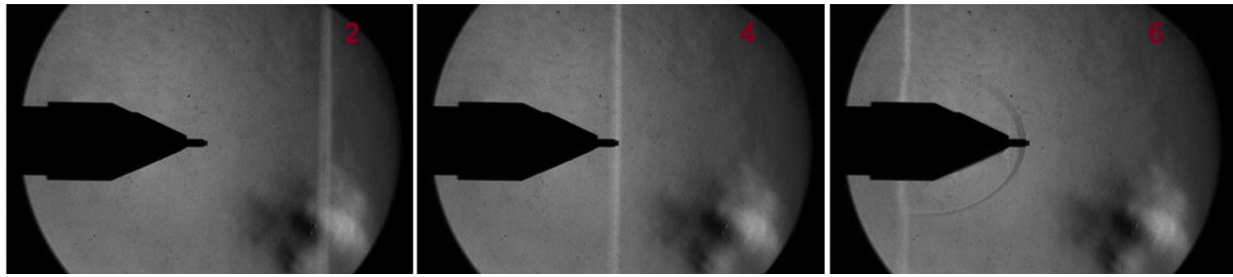


Figure 7. Movement of the starting shock for the 621-kPa run.

Figure 8 illustrates some major events in the start-up process for the 621-kPa test run. In Frame 42, supersonic flow was established around the probe, creating a bow shock. Shortly after, a wave or contact surface first appeared in Frame 44 and disappeared after Frame 52. Hence, the speed of this wave was about 798 m/s, which was on the same order of magnitude as the gas speed. According to these schlieren images, it appears that the tunnel started fully in Frame 57, and the entire start-up process took about 1.77 ms (53 frame intervals) since the arrival of the starting shock at the Pitot sensor #3.

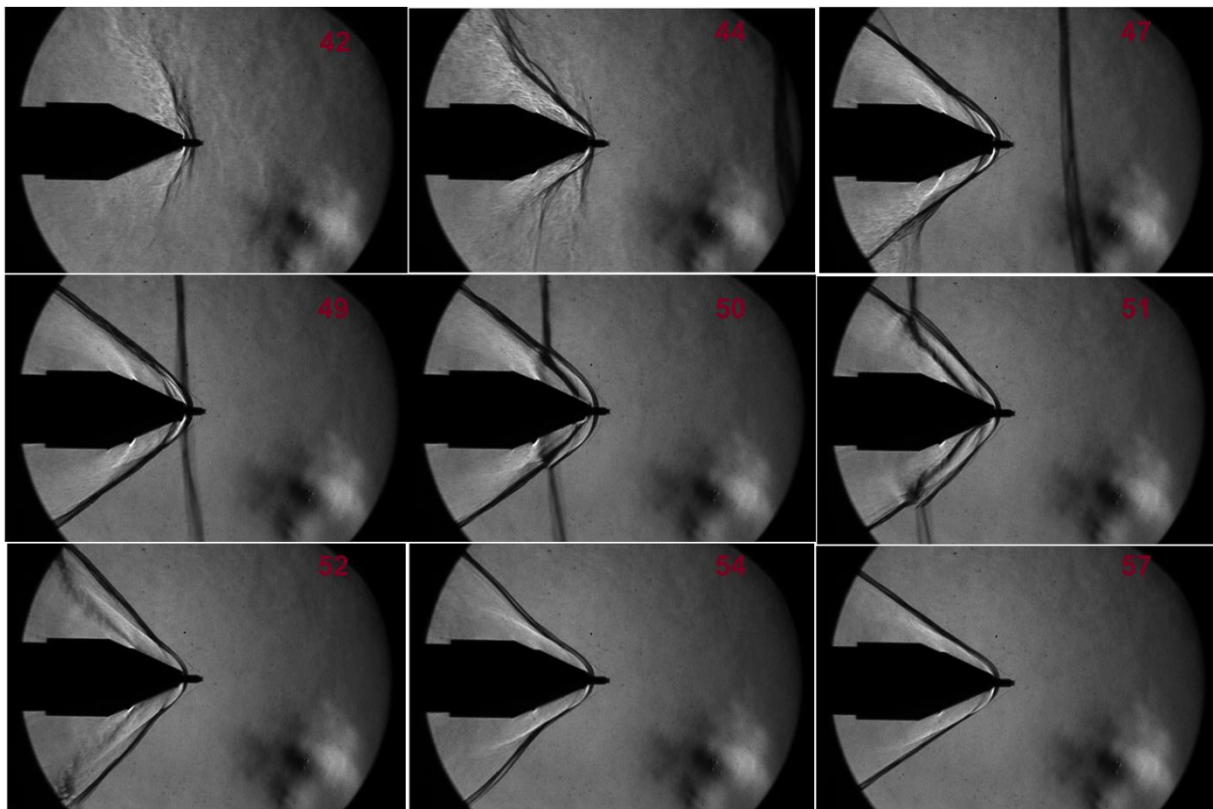


Figure 8. Sample frames during the start-up process for the 621-kPa run.

Figure 9 shows the Pitot pressure time history for the 621-kPa test run, and four events have been marked on the trace that correspond to particularly interesting frames during the start-up process. In Frame 4, the starting shock has just arrived at the Pitot sensor #3, thereby increasing the pressure significantly. The tunnel flow became supersonic at about Frame 42, and it appears that a shock was formed in front of the Pitot sensor #3, resulting in a sudden large pressure rise. The decrease in pressure 0.27 ms after this is correlated with the arrival of another wave or contact surface, as shown in Frame 49. Finally, it appears

that the tunnel started fully at 1.77 ms after the arrival of the starting shock at the Pitot sensor #3, as illustrated in Frame 57. After Frame 57, the bow shock from the Pitot rake remained stationary.

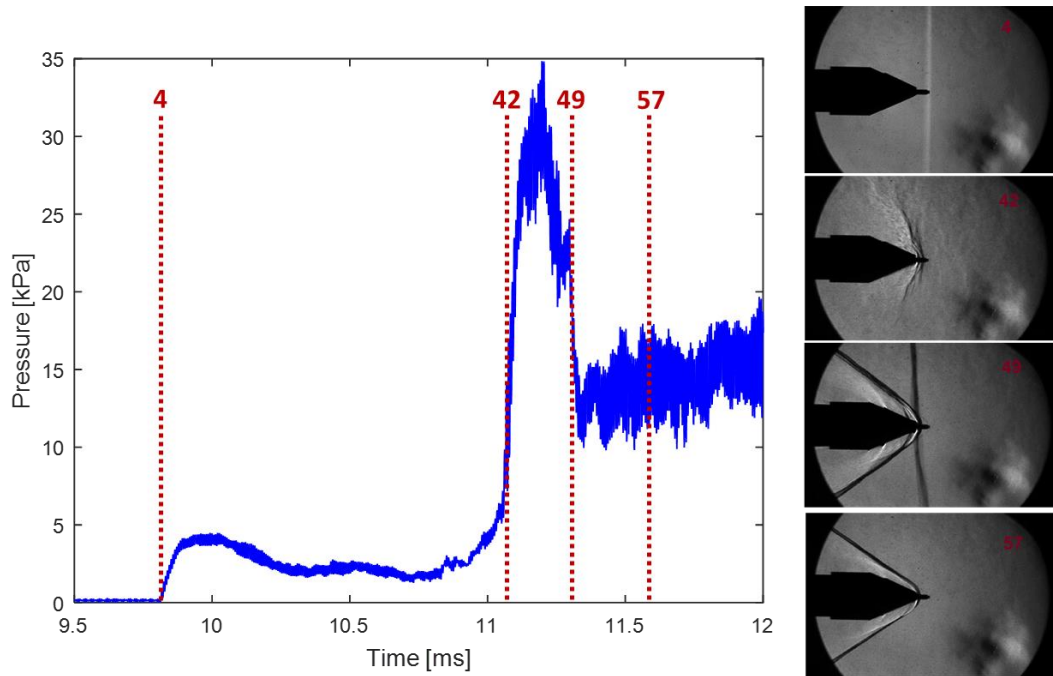


Figure 9. Pressure time history for Pitot sensor #3 (marked with 4 major events) for the 621-kPa run.

Spectral Analysis on Schlieren Images for the Pitot Rake at $P_o = 2.59 \text{ MPa}$

For hypersonic flows, the 2nd mode instability is susceptible to tunnel noise via receptivity mechanisms, thereby affecting the natural transition location significantly. Hence, it is crucial to characterize the tunnel noise (i.e., acoustic noise originated from the tunnel's nozzle wall boundary layer) prior to any boundary-layer transition experiments. In the present study, we attempted to use the schlieren images to characterize the tunnel noise based on the *density-gradient* approach; for this purpose, the Pitot rake was placed in a vertical orientation. Figure 10 shows a sample schlieren image for the Pitot rake placed in the vertical orientation during the 2.59-MPa run. Note that there were some particle impacts on the Pitot rake during the run, as illustrated in Figure 10. Additionally, a small bow shock was formed upstream of the Pitot sensor #3; this bow shock merged with the primary bow shock originating from the rake.

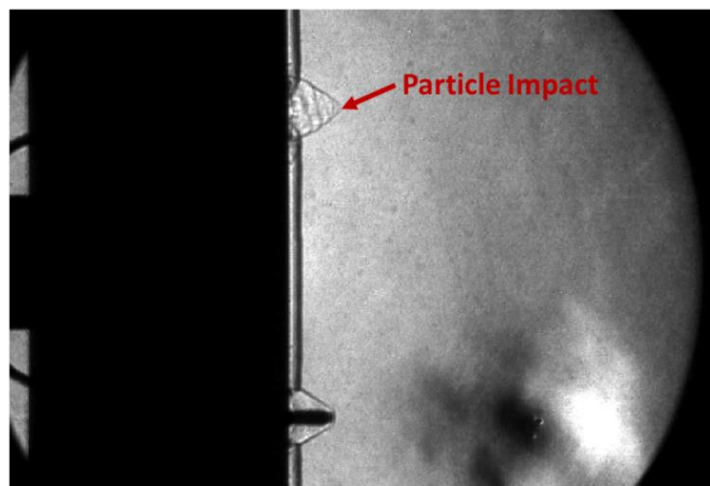


Figure 10. Schlieren image for the Pitot rake in the vertical orientation at $P_o = 2.59 \text{ MPa}$.

To measure the frequency content of the flowfield, a higher frame rate from the camera is needed. Hence, a much smaller pixel window area of 128×56 with a frame rate of 900,000 fps and a shutter time of 794 ns was selected. This smaller pixel window area covered most of the region around the Pitot sensor #3, along with the region upstream of the bow shock (freestream region). Figure 11 shows the normalized schlieren signal over a small region downstream of the bow shock (averaged over a 2×2 pixel window) for the 2.59-MPa run. Based on the schlieren signals, the tunnel started at around 100 ms, and at this point the schlieren signal became much noisier compared to the *pre-start* time period. Additionally, there was a small signal drop at $t = 210$ ms that corresponded to the arrival of the expansion fan reflected from the driver endwall, followed by another 100-ms quasi-steady period. This trend was also observed in the Pitot pressure measurements.

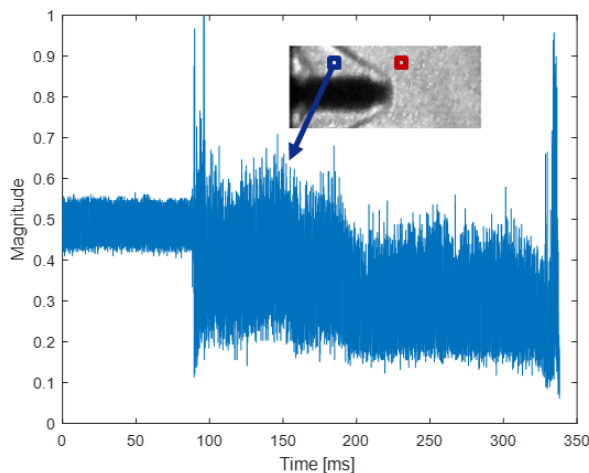


Figure 11. Plot of normalized schlieren signal vs. time over a 2×2 pixel window at $P_o = 2.59$ MPa.

Power-spectral-density (PSD) analysis was then performed on the normalized schlieren signals during the 2.59-MPa run. Figure 12 shows the frequency spectra of the flow disturbances in the regions upstream and downstream of the bow shock for the 2.59-MPa run, along with the background spectrum. Note that the locations, where the 2×2 pixel windows were selected for the regions upstream and downstream of the bow shock, are depicted as small red and blue boxes, respectively, as illustrated in Figure 11. The spectral power of the schlieren signals during the run were clearly much larger than that of the background at frequencies less than 300 kHz. This response should be sufficient to image boundary layer instabilities, which are much larger magnitude than freestream disturbances, and on the order of 300 kHz or less. The spectral power in the region downstream of the bow shock was at least an order of magnitude larger than that in the region upstream of the bow shock. This is consistent with the higher density behind the bow shock and the amplification of disturbances through the shock. As expected, the tunnel noise is typically dominated by low frequency components (at frequencies less than 300 kHz) and rolls off at higher frequencies.

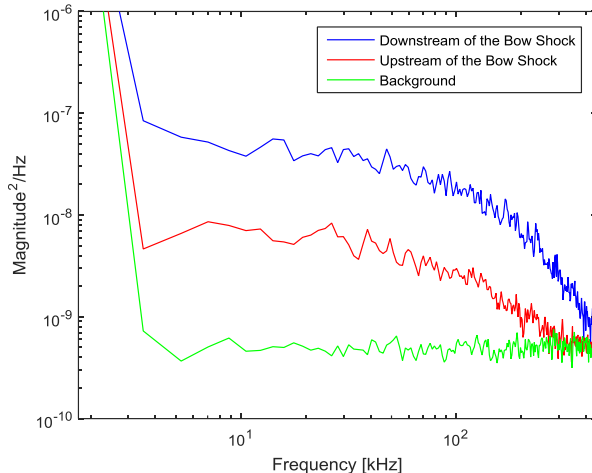


Figure 12. Power-spectral-density (PSD) analysis on schlieren signals for the 2.59-MPa run.

Schlieren Imaging Results for the Blunt Cone at $P_o = 1.38 \text{ MPa}$

The second model used in this work was a large blunt cone, as stated above. For this set of experiments, the tunnel was operated in a pneumatic-driven fast plug valve mode, and a 200-mm f/2.8 camera lens was used to visualize the flow interaction with the blunt cone model, giving a spatial resolution of 0.189 mm/pixel. A 1024×1024 pixel window was selected, and the frame rate of the camera was set at 20,000 fps with a shutter time of 1 μs . Figure 13 shows a sample schlieren image for the blunt cone at $P_o = 1.38 \text{ MPa}$, and the air was flowing from right to left. A bow shock structure was formed in front of the blunt cone with a standoff distance of about 5.9 mm (or 31 pixels); sequential frames show that the structure was stationary throughout the entire run. Note that the boundary layer growth cannot be observed from this image. The reason might be that the boundary layer thickness at this particular Reynolds number is too thin to be resolved by the camera-lens setup. In addition, the shutter time of the camera might be too high, resulting in motional blurring. Clearly, a shorter exposure time is desirable, but the limit for the camera is about 0.25 μs . Alternatively, a pulsed light source might be used. The bow shock shape can be inferred from the schlieren image and will then be compared to the shapes inferred from the two-photon Kr PLIF experiments and the US3D CFD calculations, and this comparison will be presented below (see Fig. 19).

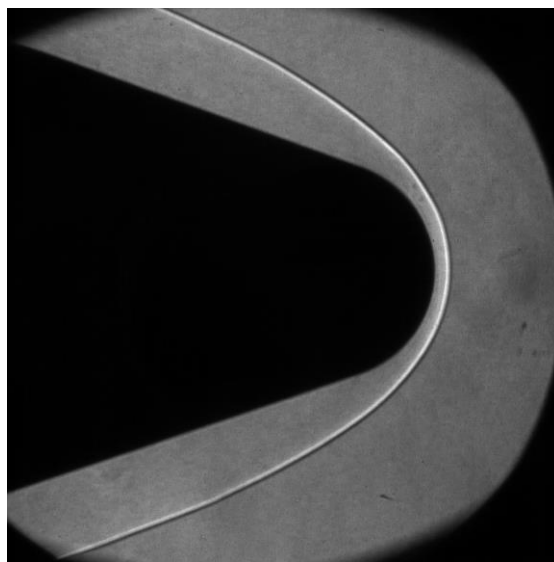


Figure 13. Schlieren image for the blunt cone at $P_o = 1.38 \text{ MPa}$.

Two-Photon Kr PLIF Imaging Result for the Blunt Cone at $P_o = 1.38 \text{ MPa}$

Two-photon Kr PLIF (at 10-Hz acquisition frequency) is the second flow visualization technique implemented in the Mach-6 Ludwieg tube. The PLIF technique has a significant advantage over the schlieren technique in that it allows for a rather narrow depth of focus (less than 0.5 mm in this study) solely due to the laser sheet thickness; this feature is particularly useful for studying or visualizing highly 3-D flow disturbances. Fluorescence signal is maximum when the laser line-center coincides with the peak of the Kr absorption line (note that there is no significant Doppler shift along the laser propagation direction). In particular, for the Mach-6 air flow, the number density ($n = 1.04 \times 10^{24} \text{ m}^{-3}$) is low, with a freestream static pressure of $P = 0.87 \text{ kPa}$ when $P_o = 1.38 \text{ MPa}$ and a freestream static temperature of $T = 61 \text{ K}$ when $T_o = 500 \text{ K}$; on the other hand, collisional quenching will also be low. Prior to the experiments, when there were trace amounts of Kr remaining in the test section (at $P = 0.41 \text{ kPa}$) from the previous run, the dye laser beam was first tuned to the wavelength near 544.03 nm (confirmed with a wavemeter), followed by scanning the dye laser in small, incremental steps and seeking for the brightest fluorescence signals collected by the camera to ensure that the 214.7-nm light was at the peak of the Kr absorption line. Additionally, it appears that fluorescence signal-to-noise ratios (SNR) larger than 10 can be obtained when seeding the air with 2.5% Kr. Hence, for this set of experiments, the hot air in the driver tube was seeded with 2.5% Kr.

Two-photon Kr PLIF was used to image the bow shock from the blunt-cone model; here, the tunnel was operated in the fast plug valve mode. Since the run time for the tunnel is typically 200 ms, two PLIF images can be acquired per run, and the images shown in this section were taken during the second quasi-steady period. Figure 14 shows a sample Kr PLIF raw image (on the left) using a 7.1-mm wide laser sheet (with a laser energy of $\sim 3 \text{ mJ/pulse}$) for the 1.38-MPa run (seeded with 2.5% Kr). Note that the flow direction in these PLIF images is from top to bottom. The upper edge of the laser sheet on the image was located at a distance of $\sim 7 \text{ mm}$ downstream of the nose tip. The cone surface, shock layer, and freestream regions can easily be identified from the raw image. Note that the signal counts in the freestream region were not uniform, and the signal counts appeared to be brighter on the right side (or at about 130 pixels or 4.6 cm away from the cone surface in the spanwise direction). This is due to the fact that the focus of the laser sheet was not at the cone surface but at a location of 4.6 cm away from the cone surface. A different spherical convex lens with a slightly longer focal length is needed to get higher SNR in the future. Based on the raw image, the signal counts (or the photo-electrons) in the shock layer and the freestream are around 230 counts (2760 e⁻) and 100 counts (1200 e⁻), respectively. Figure 14 (on the right) also presents a processed image after correcting for laser sheet non-uniformity and normalizing with the freestream values. Multiple runs at locations near the nose tip were performed, and the bow shock radii at these locations can be inferred from these images and compared to the measured values from the schlieren image (see Fig. 19).

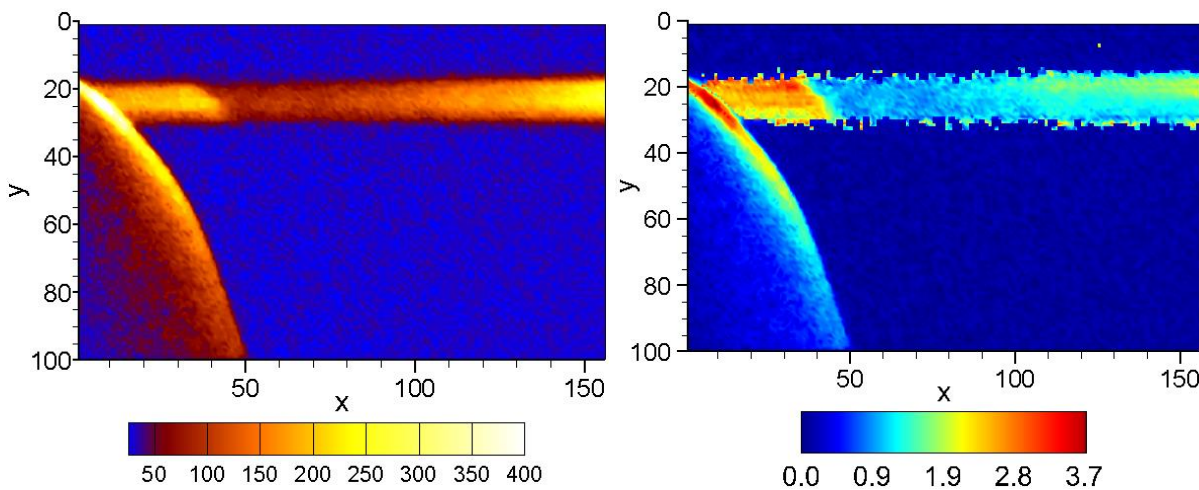


Figure 14. Kr PLIF raw image (left) and corrected image (right) using a 7.1-mm wide laser sheet.

Our second objective was to image the middle section of the blunt cone with a much larger (i.e., taller) laser sheet. We wanted to investigate how tall the laser sheet can be with acceptable signals in the Mach-6 flow. The laser sheet focus happened to be at the surface of the middle section of the large blunt cone. This is quite crucial because the fluorescence signal (per pixel) drops quadratically for two-photon absorption process when laser intensity (per pixel) decreases, and we want the interrogation region to be at the laser sheet focus. The total laser energy of the 214.7-nm beam was maintained at around 3 mJ/pulse during the experiment. Figure 15 (on the left) shows the Kr PLIF raw image after widening the laser sheet from 7.1 mm to 28 mm for the 1.38-MPa run. It should also be noted that the hot air in the driver tube was seeded with 5% Kr for this particular 1.38-MPa run (in order to improve fluorescence signals). The upper edge of the laser sheet on the image was located at a distance of ~13.6 cm downstream of the nose tip. Note that the 28-mm wide laser sheet appears to be less uniform than the 7.1-mm wide sheet, perhaps due to some misalignment. Nevertheless, the cone surface, shock layer, and freestream can be observed from the image, and the signal counts (or the photo-electrons) for the shock layer and freestream regions are around 100 counts (1200 e⁻) and 50 counts (600 e⁻), respectively, along the row at $y = 200$ pixels. Figure 15 (on the right) also presents the processed Kr PLIF image after correcting for laser sheet non-uniformity and normalizing with the freestream values. It appears that the 28-mm wide laser sheet with a laser energy of 3 mJ/pulse can give sufficient fluorescence signals for data processing. As stated in the experiment setup section, the injection seeder for the Nd:YAG laser was not operating properly for this set of measurements; with better operation of the injection seeder, pulse energy > 10 mJ is possible, which should enable interrogation regions of several centimeters tall. In addition, spatial resolution should be improved for future work (through the use of different laser and camera optics), as it was too coarse in these measurements to resolve the boundary layer.

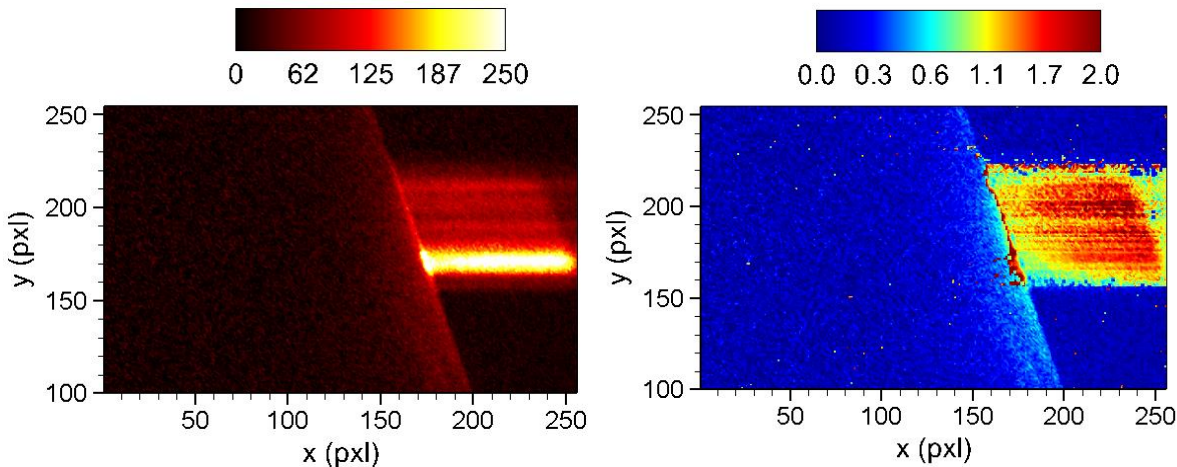


Figure 15. Kr PLIF raw image (left) and corrected image (right) using a 28-mm wide laser sheet.

US3D CFD Calculation for the Blunt Cone at $P_o = 1.38$ MPa

Computational simulations were performed using US3D, a high-fidelity unstructured finite-volume code. The code is equipped with low-dissipation flux routines and hybrid RANS/LES turbulence models to investigate the unsteady, high-Reynolds-number applications being considered. In this case, RANS simulations were computed using the compressible form of the Spalart-Allmaras One-Equation Model contained within US3D. The simulations were performed locally on a 64-bit Linux desktop computer with 31.2 GB of memory. Computations were run in parallel using 8 Intel® Core™ i7-4790 processors each at 3.60 GHz.

The grid for the computational simulations was generated using GridPro, a commercial grid generation software for creating structured, multi-block hexahedral element grids. To limit the expense, a standard axisymmetric grid, containing approximately 116000 cells was used. The overall grid distribution for the

simulations is shown in Figure 16. Wall clustering of the cells to the cone surface was performed using the internal algorithms in GridPro in order to resolve the boundary layer and ensure a y^+ of less than 1, as shown in Figure 17. The entire length of the model was simulated to allow the boundary layer to develop and transition naturally. Inflow conditions were set assuming a P_0 of 1.38 MPa, T_0 of 505 K, and a Mach number of 6. The wall of the cone was assumed to be adiabatic and the flow medium was assumed to be air as a perfect gas. The symmetry plane and sidewalls of the domain were set to symmetry boundary conditions, and the plane at $x = x_{\max}$ was set to supersonic outflow. Note the the flow direction for the simulations is from left to right.

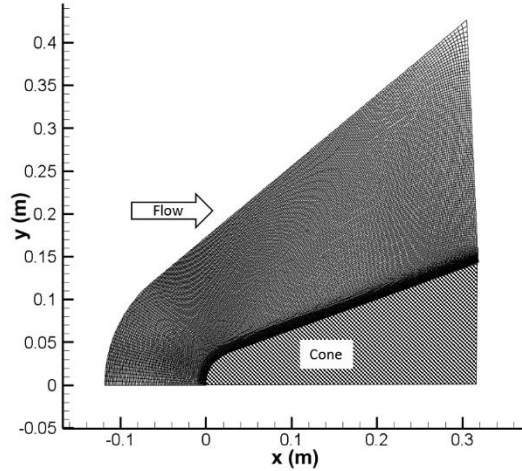


Figure 16. Overall grid distribution for US3D simulation for the blunt cone.

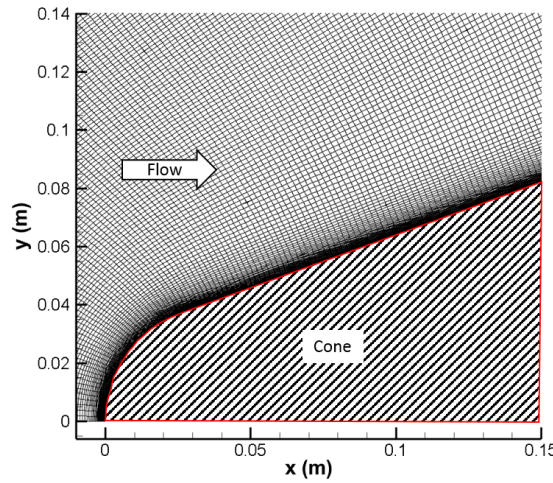


Figure 17. Zoomed-in grid distribution (for the region near the cone surface) for US3D simulation.

Figure 18 shows a simulated 2-D density contour plot. The density contour plot clearly shows the freestream, the shock layer, and the boundary layer regions. The simulated densities for the freestream, the region immediately behind the normal shock (at the nose tip), and the regions in the shock layer (right behind the bow shock) at $x = 7$ mm and 13.6 cm are about 0.06, 0.26, 0.22, and 0.15 kg/m^3 , respectively. Here, we also wanted to perform a quick comparison between the simulation and the PLIF measurements at two different axial locations ($x = 7$ mm and 13.6 cm). The simulation gives the density ratios of the shock layer to the freestream of 3.67 and 2.5 at $x = 7$ mm and 13.6 cm, respectively. The signal count ratios of the shock layer to the freestream from the PLIF measurements are about 2.3 and 2 at $x = 7$ mm and 13.6 cm, respectively. Note that Kr fluorescence signal depends on the number density, the collisional

quenching (a function of temperature and pressure), and the lineshape effects. By properly accounting for the collisional quenching and the lineshape effects, the inferred density ratios from the PLIF experiments should be in a closer agreement with the simulated values. We will address such quantitative comparison more in the future.

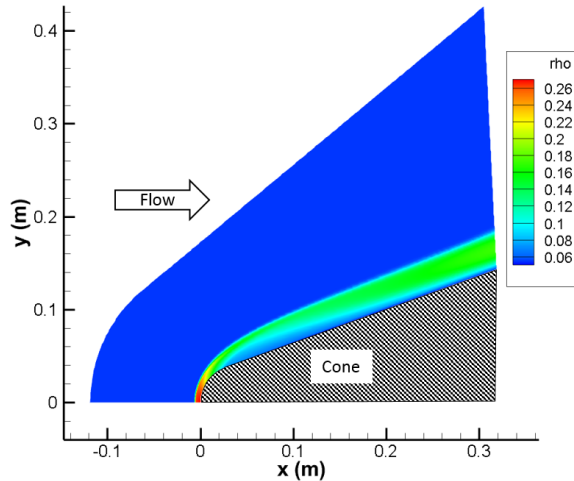


Figure 18. 2-D density contour plot for the blunt cone model at $P_0 = 1.38$ MPa.

Figure 19 shows a comparison of the bow shock shapes between two flow visualization techniques and the US3D simulation. In general, excellent agreement on the overall shapes between the schlieren and the simulation can be found. In addition, the measured bow shock radii from the Kr PLIF experiments at the locations near the nose tip agree reasonably well with the schlieren and the simulation, but are consistently 7.4% smaller at the locations of 13.6 cm or more downstream of the nose tip. Such discrepancy is partially due to the fact that the acquired image only covers a small section of the blunt cone without including the nose tip, thereby introducing a larger uncertainty of the actual axial location along the cone. Also, as shown in Figure 15, the boundary between the shock layer and freestream regions is less defined, resulting in an uncertainty of the bow shock location. Here, we simply assume that the shock is located at the pixel where the gradient of the signal count is at its maximum.

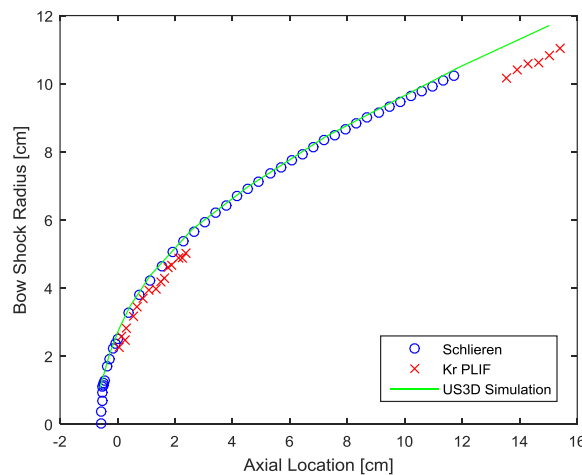


Figure 19. Comparison of bow shock shapes between flow visualization techniques and CFD calculation.

IV. Conclusions

High-speed schlieren and two-photon Kr planar laser-induced fluorescence (PLIF) were implemented in the new AFRL Mach-6 Ludwieg Tube Hypersonic Wind Tunnel. High-speed schlieren was first used to image the startup process during the 621-kPa run, and the acquired images helped interpret the pressure measurements during the startup process. In addition, a much faster frame rate (i.e., 900,000 fps) with a smaller interrogation window was used to capture any high-frequency flow disturbances and derive frequency spectra during the 2.59-MPa run. Next, high-speed schlieren and two-photon Kr PLIF were used to image the bow shock shape from the large, 19.5-deg. half-angle blunt cone with a nose radius of 3.96 cm, a total length of 31.8 cm, and a base diameter of 28.7 cm at $P_0 = 1.38$ MPa. The bow shock shape was inferred from these two measurement techniques. CFD calculations employing the US3D simulation code were also performed, and the simulated bow shock shape was then compared to the measurements. Excellent agreement on the bow shock shapes among the flow visualization techniques and the simulation were found.

Acknowledgments

The authors would like to thank Dr. Matthew P. Borg (AFRL/RQHF) for his assistance in operating the Mach-6 Ludwieg tube. The authors would like to thank Benjamin Hagen (AFRL/RQV) for his support on the development of high-speed schlieren system. This work was supported by Ivett Leyva of AFOSR. The authors also acknowledge the help from Dr. Pramod Subbareddy for using the US3D code. Support for Joshua D. Pickles was made possible by Army Grant W911NF-16-1-0072.

References

- ¹W. S. Saric, H. L. Reed, and E. J. Kerschen. Boundary-layer receptivity to freestream disturbances. *Annual Review of Fluid Mechanics*, 34:291-319, 2002.
- ²S. P. Schneider. Developing mechanism-based methods for estimating hypersonic boundary-layer transition in flight: the role of quiet tunnels. *Progress in Aerospace Sciences*, 72:17-29, 2015.
- ³L. M. Mack. Linear stability theory and the problem of supersonic boundary-layer transition. *AIAA Journal*, 13:278-289, 1975.
- ⁴S. J. Laurence, A. Wagner, K. Hannemann, V. Wartemann, H. Lüdeke, H. Tanno, and K. Itoh. Time-resolved visualization of instability waves in a hypersonic boundary layer. *AIAA Journal*, 50:243-246, 2012.
- ⁵S. J. Laurence, A. Wagner, and K. Hannemann. Schlieren-based techniques for investigating instability development and transition in a hypersonic boundary layer. *Exp. Fluids*, 55:1782-1789, 2014.
- ⁶K. M. Casper, S. J. Beresh, J. F. Henfling, R. W. Spillers, and B. O. M. Pruett. High-speed Schlieren imaging of disturbances in a transitional hypersonic boundary layer. 51st AIAA Aerospace Sciences Meeting, AIAA paper 2013-0376, January 2013.
- ⁷K. M. Casper, S. J. Beresh, R. M. Wagnild, J. F. Henfling, R. W. Spillers, and B. O. M. Pruett. Simultaneous pressure measurements and high-speed Schlieren imaging of disturbances in a transitional hypersonic boundary layer. 43rd Fluid Dynamics Conference, AIAA paper 2013-2739, June 2013.
- ⁸C. P. VanDercreek, M. S. Smith, and K. H. Yu. Focused Schlieren and deflectometry at AEDC hypervelocity wind tunnel No. 9. 27th AIAA Aerodynamic Measurement Technology and Ground Testing Conference, AIAA paper 2010-4209, June 2010.
- ⁹V. Narayanaswamy, R. Burns, and N. T. Clemens. Kr-PLIF for scalar imaging in supersonic flows. *Opt. Lett.* 36:4185-4187, 2011.
- ¹⁰A. G. Hsu, V. Narayanaswamy, N. T. Clemens, and J. H. Frank. Mixture fraction imaging in turbulent non-premixed flames with two-photon LIF of Krypton. *Proc. Combust. Inst.* 33:759-766, 2011.
- ¹¹D. Zelenak, W. Sealy, and V. Narayanaswamy. Collisional broadening of Kr transition with combustion species as collision partners. *JQSRT* 174:28-38, 2016.
- ¹²R. A. Burns, H. Koo, N. T. Clemens, and V. Raman. Experimental and computational studies of mixing in supersonic flow. 41st AIAA Fluid Dynamics Conference and Exhibit, AIAA paper 2011-3936, June 2011.
- ¹³J. L. Palmer, A. F. P. Houwing, M. C. Thurber, S. D. Wehe, and R. K. Hanson. PLIF imaging of transient shock phenomena in hypersonic flows. 18th AIAA Serospace Ground Testing Conference, AIAA paper 94-2642, June 1994.
- ¹⁴N. J. Parziale, M. S. Smith, and E. C. Marineau. Krypton tagging velocimetry of an underexpanded jet. *Appl. Opt.* 54:5094-5101, 2015.
- ¹⁵D. Zahradka, N. J. Parziale, M. S. Smith, and E. C. Marineau. Krypton tagging velocimetry in a turbulent Mach 2.7 boundary layer. *Exp. Fluids* 57:62, 2016.
- ¹⁶N. Jiang, M. Webster, W. R. Lempert, J. D. Miller, T. R. Meyer, C. B. Ivey, and P. M. Danehy. MHz-rate nitric oxide planar laser-induced fluorescence imaging in a Mach 10 hypersonic wind tunnel. *Appl. Opt.* 50:A20-A28, 2011.
- ¹⁷R. L. Kimmel, M. Borg, J. S. Jewell, K.-Y. Lam, R. Bowersox, and S. Fuchs. AFRL Ludwieg Tube Initial Performance. 55th AIAA Aerospace Sciences Meeting, AIAA paper, January 2017, in preparation.

¹⁸G. S. Settles. Schlieren and Shadowgraph Techniques. Springer-Verlag, 2001.

¹⁹D. R. Jonassen, G. S. Settles, and M. D. Tronosky. Schlieren “PIV” for turbulent flows. *Optics and Lasers in Engineering* 44:190-207, 2006.